Atomic force spectroscopy and density-functional study of graphene corrugation on Ru(0001)

Elena Voloshina*
Humboldt-Universität zu Berlin, Institut für Chemie, 10099 Berlin, Germany

Yuriy Dedkov†
SPECS Surface Nano Analysis GmbH, 13355 Berlin, Germany and IHP, Im Technologiepark 25, 15236 Frankfurt (Oder), Germany
(Received 21 January 2016; revised manuscript received 19 May 2016; published 13 June 2016)

Graphene, the thinnest material in the world, can form moiré structures on different substrates, including graphite, *h*-BN, or metal surfaces. In such systems, the structure of graphene, i.e., its corrugation, as well as its electronic and elastic properties, are defined by the combination of the system geometry and local interaction strength at the interface. The corrugation in such structures on metals is heavily extracted from diffraction or local probe microscopy experiments, and it can be obtained only via comparison with theoretical data, which usually simulate the experimental findings. Here we show that graphene corrugation on metals can be measured directly employing atomic force spectroscopy, and the obtained value coincides with state-of-the-art theoretical results. The presented results demonstrate an unexpected space selectivity for the $\Delta f(z)$ signal in the atomic force spectroscopy in the moiré graphene lattice on Ru(0001), which is explained by the different response of the graphene layer on the indentation process. We also address the elastic reaction of the formed graphene nanodoms on the indentation process by the scanning tip that is important for the modeling and fabrication of graphene-based nanoresonators on the nanoscale.

DOI: 10.1103/PhysRevB.93.235418

I. INTRODUCTION

Graphene superlattices [1–4], and among them graphene-based moiré structures, have attracted increased attention in recent condensed-matter studies because they can be used as a foundation for tailoring the transport properties of heterosystems [1–3]. The formation of ordered commensurate moiré structures of graphene on different substrates leads to the cloning of Dirac cones in reciprocal space, which in turn modifies the electronic spectrum of carriers via the opening of minigaps around the Dirac point, deviates the energy band dispersion from the linear one, changes the effective mass and velocity of the carriers, etc. [1–6]. All these effects are a manifestation of the additional large-scale modulation potential originating from the moiré superlattice, which usually has a size of several nanometers.

The existence of moiré structures on the basis of graphene has been known for many years, and they were successfully imaged by means of a scanning tunneling microscope for graphene on common graphite [7,8] and graphene on Si- or C-faced SiC [9,10]. Here graphene moiré structures appear naturally during the preparation of these systems for experiment due to the weak interaction between single graphene layers. The periodicities, as well as corrugations of such graphene moiré structures, are defined by the misalignment angle between two carbon lattices in the neighboring graphene layers. Recent experiments on the transport properties of ultraflat graphene in artificial graphene/h-BN heterostructures revealed the modified massless electronic spectrum of graphene. The moiré-lattice-related Dirac points in the electronic structure of graphene appear as local dips in the scanning tunneling microsope spectroscopy data [3] (the dI/dV signal is proportional to the local density of states). They are revealed via observation of the so-called Hofstadter butterfly "self-similar" superlattice energy spectrum [1,2] for a charge particle moving under the simultaneous influence of two periodic potentials, namely atomic-lattice- and moiré-lattice-related potentials, and a magnetic field.

One of the moiré lattice classes is a graphene layer on the close-packed surfaces of 4*d* and 5*d* transition metals, such as Ir(111), Pt(111), or Ru(0001) [11,12]. Such graphene-metal systems are the subject of long-term surface-science studies, and they were proposed as substrates for ordered arrays of metallic clusters, which can then be used in storage technology or in catalysis as the behavior of a cluster's array could be modeled on the basis of a single element. The electronic or magnetic properties of such cluster arrays depend strongly on the underlying graphene-metal substrate. The crystallographic structure of these graphene-metal systems, and hence their electronic properties, are defined by the lattice mismatch of graphene and a metal surface as well as by the strength of the local interaction at the interface, leading to the observation of various moiré structures with different corrugations even for the same graphene-metal combinations [13–15]. Thus precise knowledge of the crystallographic structure of the graphene-metal system is crucial for the modeling of its electronic properties. Macroscopic diffraction experiments, such as low-energy electron diffraction (LEED), or local probe methods, such as scanning tunneling microscopy (STM) and atomic force microscopy (AFM), can provide information about the symmetry of the system and the lattice alignment of graphene and metal [16–18]. The graphene moiré lattice corrugation on metal is extracted from a comparison of experimental and theoretical data, e.g., from the modeled STM images at different bias voltages [14,17,19] or from simulated $I(V)$ curves in LEED experiments [16,18]. In principle, AFM can do this job, but as was shown, the correct topography in this case is influenced by the residual electrostatic forces

*elena.voloshina@hu-berlin.de
†dedkov@ihp-microelectronics.com; yuriy.dedkov@icloud.com

between the tip and the sample [20]. In such AFM experiments, compensation of the local contact potential difference variation over the moiré lattice is not a trivial task. Also, because graphene is a very elastic material, the imaged topography in AFM experiments can be influenced by the indentation effect from the tip, which is placed in close vicinity to the surface [21,22]. Therefore, the necessity of the tool, which gives full information about graphene moiré, is obvious, and our approach is based on complementary STM and AFM spectroscopy measurements in this case.

II. COMPUTATIONAL AND EXPERIMENTAL DETAILS

A. DFT calculations

Density-functional theory (DFT) calculations were carried out using the projector augmented wave (PAW) method [23], a plane-wave basis set, and the generalized gradient approximation as parametrized by Perdew *et al.* [24] and as implemented in the VASP program [25]. The plane-wave kinetic-energy cutoff was set to 400 eV. The long-range van der Waals interactions were accounted for by means of the DFT-D2 approach [26]. The supercell used to model the graphene-metal interface has a (12×12) lateral periodicity with respect to Ru(0001) [Fig. 1(a)]. It is constructed from a slab of three layers of Ru atoms with a (13×13) graphene layer adsorbed from both sides. The W tip is modeled with a 32-atom (i.e., 1−4−9−4−9−4−1) cluster. Thus our structural model [see Figs. 1(b) and 1(c)] is completely symmetric with respect to the middle layer of the slab and the middle layer of the W cluster. During the structure relaxation, the positions of the carbon atoms (x,y,z coordinates) as well as the apex W atoms (z coordinate) are allowed to relax. The surface Brillouin zone is sampled with a single k-point at the Γ-point. The STM images are calculated using the Tersoff-Hamann formalism [27] for the fully relaxed graphene/Ru(0001) slab with five Ru layers and (3×3×1) sampling in the Brillouin zone.

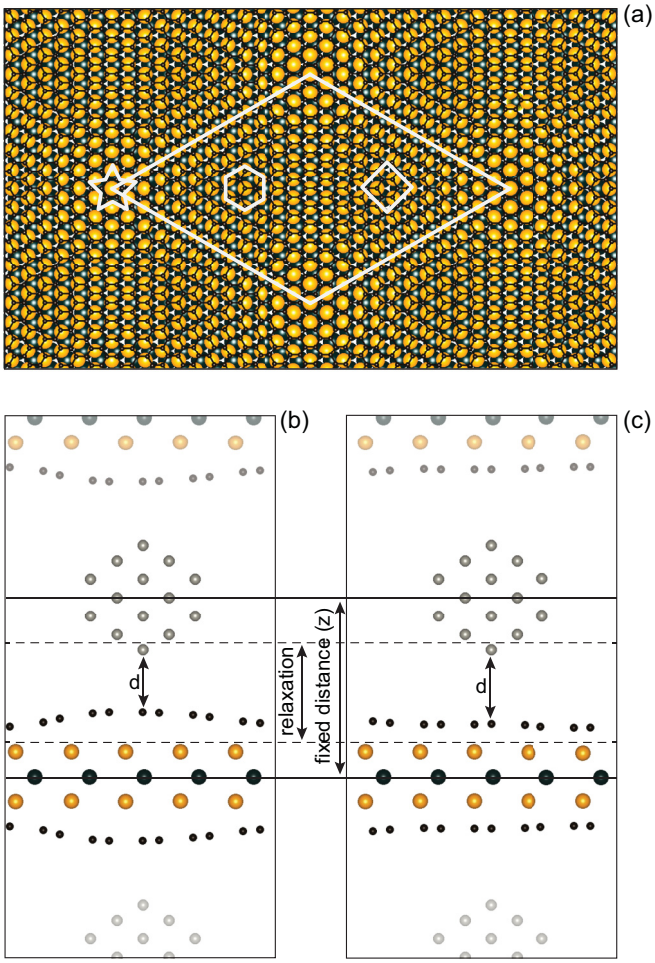

FIG. 1. (a) Top view of graphene/Ru(0001). The moiré unit cell is denoted by a large rhombus, and the respective high-symmetry places are marked by a white star (ATOP), a hexagon (HCP), and a small rhombus (FCC). Parts (b) and (c) show the schematic representation of the geometry for the ATOP and FCC places, respectively, of the W-tip/graphene/Ru(0001) model used in the simulations of the interaction energy curves.

B. STM and AFM experiments

The STM and AFM measurements were performed in constant current, constant frequency shift, or constant height modes, respectively. In the first two cases, the topography of the sample, $z(x,y)$, was studied with the corresponding signal, namely the tunneling current (I_T) or the frequency shift (Δf), used as an input for the feedback loop. In the last case, the feedback was completely switched off, and I_T, Δf, and dissipation (ΔU) signals were collected in the atom-tracking mode allowing for the thermal drift compensation for the tip z-position. z-spectroscopy data were recorded on a grid of (96×96) or (128×128) pixels, and the topography of the sample was recorded simultaneously, allowing us to obtain the "$z = 0$" reference point used in the data treatment as well as for the careful tracing of the drift in the xy plane. All STM/AFM data were collected at room temperature with SPM Aarhus 150 equipped with KolibriSensor™ from SPECS GmbH with a Nanonis Control system. In these measurements, a sharp W tip was used, which was cleaned *in situ* via Ar^+ sputtering. In the presented STM images, the tunneling bias voltage, U_T, is applied to the sample and the tunneling current, I_T, is collected through the tip, which is virtually grounded. During the AFM measurements, the sensor was oscillating with a resonance frequency of $f_0 = 998\,666$ Hz and a quality factor of $Q = 22\,500$. The oscillation amplitude was set to $A = 200$ or 300 pm. Base pressure during all experiments was below 8×10^{-11} mbar.

C. Sample preparation

Prior to every set of the experiment, the Ru(0001) substrate was prepared via cycles of the Ar-ion-sputtering and annealing. The graphene/Ru(0001) system was prepared in an ultrahigh-vacuum system via cracking of ethylene: $T = 1020$ K, $p = 2\times10^{-7}$ mbar, and $t = 30$ min. This procedure leads to the single-domain graphene layer on Ru(0001) of very high quality, which was verified by means of STM and AFM (see Fig. S1 of the Supplemental Material [28]).

III. RESULTS AND DISCUSSION

Graphene on Ru(0001) is the most representative case of the strongly corrugated graphene-metal system. It is a subject of intensive studies due to its crystallographic and electronic structure [29–33]. Graphene on Ru(0001) can be considered as a periodic sequence of the alternating positions of the different stacking of graphene on metal substrate. Here, the labels for the high-symmetry positions of the moiré structure are determined based on the adsorption positions of Ru(0001), which are the centers of the carbon rings: ATOP, FCC, and HCP [see Fig. 1(a) and the inset of Fig. 2(a)]. Such different local atom stackings of carbon and metal atoms lead to the modulation of the interaction strength at the interface, yielding the formation of a strongly corrugated graphene layer on Ru(0001) with the height difference between two limit positions of 127 pm as deduced from our DFT calculations. The natural approach of using STM or AFM to measure true corrugation does not work here, as the variation of the local density of states leads to a strong dependence of the apparent corrugation on the bias voltage between the tip and the sample [14,17,19], or because the graphene nanodoms can be modified via local chemical interaction with the apex of the tip [21,22]. In addition, the elastic properties of graphene nanodoms in the moiré structure on Ru(0001) are expected to be much different from those measured on the larger scale (μm or several tens of nm) in recent STM and AFM experiments [33–35].

If a scanning metallic tip is placed above one of the high-symmetry positions of the graphene moiré structure, then one can expect that the interaction energy between the tip and graphene will be described by the Morse or the Lennard-Jones (LJ) potential (see the respective discussion in the Supplemental Material [28]). Both of them consist of attractive and repulsive parts, which are more effective on long and short distances between objects, respectively. We calculated the interaction energy between our model tip and graphene/Ru(0001), varying the distance between the apex of the tip and graphene (for details, see the Supplemental Material). Here, distance z denotes the interval between the middle W layer of the model tip and the middle Ru layer in the graphene/Ru(0001) slab [see Figs. 1(b) and 1(c)]. Such computational experiments model the real AFM force-spectroscopy measurements. For HCP or FCC locations, we obtain the expected curves for the tip-sample interaction energy [top panel of Fig. 2(a)] with a shape that is very close to that for the Morse or LJ potential. The minimum value for the interaction energy at the FCC place is $E = -1.26$ aJ at $z = 1$ nm.

Surprisingly, the calculated curve for the interaction energy for the ATOP position shows a clear depression around $z = 1.2$ nm on the attractive part [point 4 in Fig. 2(a); the distance between the W atom of the tip apex and the C atom underneath is 227 pm] followed by the global minima for the energy of $E = -1.02$ aJ at $z = 1.01$ nm [point 6 in Fig. 2(a); the distance between the W atom of the tip apex and the C atom underneath is 211 pm]. This effect is explained by the

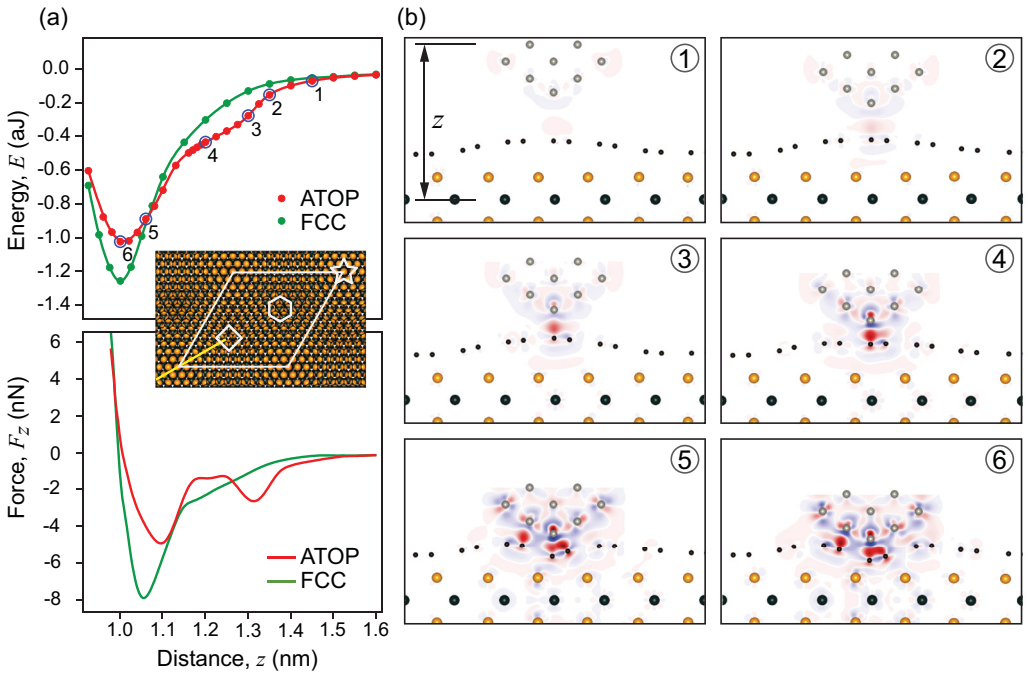

FIG. 2. Theoretical modeling of the tip-graphene interaction in AFM. (a) Interaction energy (E) calculated at two different places of graphene/Ru(0001) (top panel) and the respective tip-sample interaction force (F_z) (bottom panel) as functions of the tip-sample distance (z). The inset shows the top view of the graphene/Ru(0001) structure (white star, hexagon, and rhombus mark ATOP, HCP, and FCC places, respectively). (b) Series of snapshots of the atomic configurations corresponding to the interaction of W-tip with graphene/Ru(0001) at the ATOP place taken for six different distances indicated with numbers 1–6 at the top panel of (a). The cut is made perpendicular to the sample surface through the yellow line as shown in the inset of (a). Each structure is overlaid with the calculated difference electron density, $\Delta\rho = \rho_{\text{tip+sample}}(r) - [\rho_{\text{tip}}(r) + \rho_{\text{sample}}(r)]$. Red (blue) indicates accumulation (depletion) of the electron density. The scale is identical for each subplot and ranges from -0.03 to $+0.03$ $e/\text{Å}^3$.

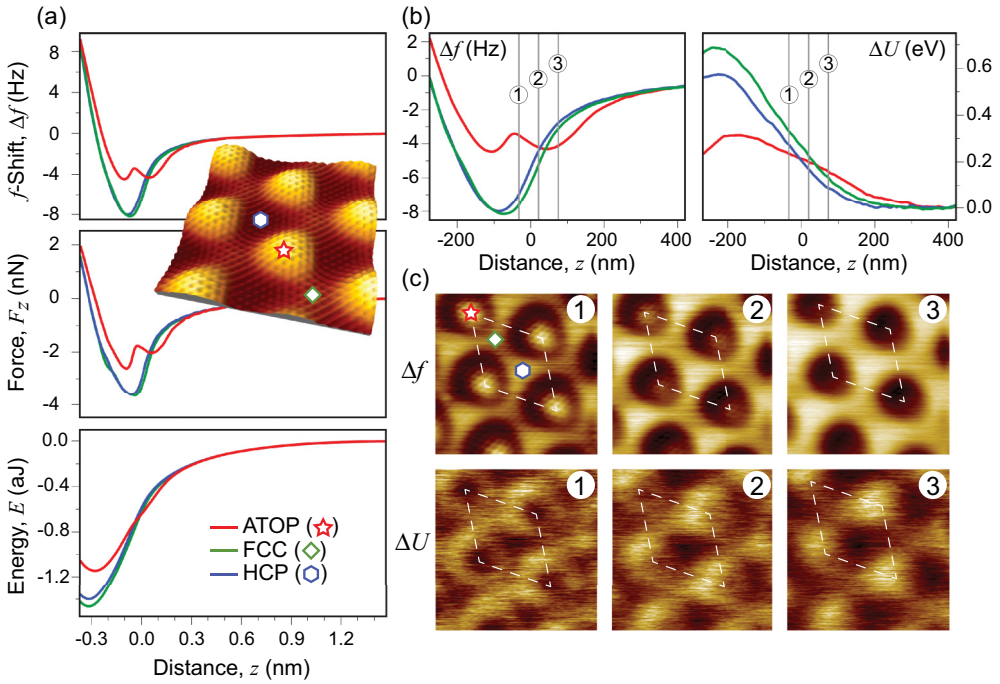

FIG. 3. Force-distance spectroscopy and constant-height scanning probe microscopy (SPM) of graphene/Ru(0001). (a) Frequency shift as a function of the tip-sample distance (Δf) measured at different places of graphene/Ru(0001) (top panel) and the respective tip-sample interaction force (F_z) and energy (E) are shown in the middle and the bottom panels. The inset shows the 3D view of the STM image of graphene/Ru(0001) with high-symmetry positions of the moiré structure marked by the corresponding symbols. Imaging parameters: 6.4×6.4 nm^2, $U_T = +0.05$ V, $I_T = 5$ nA. (b) Frequency shift (Δf) and dissipation (ΔU) signals zoomed for the tip-sample distances corresponding to the short-range interactions. (c) Series of constant-height SPM images (Δf and ΔU signals) measured at the z positions marked in (b). Minimum (dark) and maximum (bright) limits for the respective measurement channel can be extracted from the panel (b). Imaging parameters: 6.4×6.4 nm^2, $U_T = +0.05$ V, and $A = 200$ pm.

drumlike behavior of the ATOP positions of graphene moiré on Ru(0001). Indeed, if the tip is approaching the graphene bubble at the ATOP position, first it interacts with a graphene layer, and this interaction can be described by the Morse or LJ potential and can be assigned to the formation of the W-C bond at the short distance between the apex of the tip and the graphene layer [Fig. 2(b), panels 1–4]. However, it is possible to press with the tip on a graphene layer further until the strong repulsive interaction between graphene and the underlying Ru prevents further graphene flexure. This complex behavior leads to the appearance of the global minimum on the curve for the interaction energy between the tip and graphene at the ATOP position, and it leads to the formation of several W-C bonds between the tip and graphene [Fig. 2(b), panels 4–6]. Movie S1 (Fig. S2) of the Supplemental Material [28] presents a series of snapshots of the system geometry, overlaid with the charge-density distribution, obtained during the indentation process. Decomposition of the total curve for the ATOP position on two curves describing the Morse or LJ potential is not possible as it involves interaction between three objects: a scanning tip, a graphene layer, and the Ru(0001) substrate. Differentiation of the curves for the interaction energy, $F_z = -dE/dz$, gives the curves for the force, which acts on the scanning tip, for different positions of the graphene/Ru(0001) moiré structure [bottom panel of Fig. 2(a)], and these curves can be directly compared with the results of AFM spectroscopy experiments.

To verify these theoretical predictions, combined STM/AFM experiments were performed. We prepared graphene on Ru(0001) in the usual fashion via decomposition of the ethene gas at 1020 K. The representative STM topography of the as-prepared graphene/Ru(0001) moiré structure is shown in the inset of Fig. 3(a) (see also Fig. S1 of the Supplemental Material [28]), where all high-symmetry positions are clearly resolved and identified. These results are in perfect agreement with our simulated STM images obtained in the framework of the Tersoff-Hamann formalism [27] on the basis of DFT calculations (see Fig. S3 of the Supplemental Material [28]). Our combined scanning probe microscopy/spectroscopy experiments were performed with the oscillating conductive tip (resonance frequency f_0), allowing us to measure tip-graphene interaction force as a function of distance. Interaction between tip and surface leads to a slight change of the resonance frequency, and this frequency shift $\Delta f(z)$ signal is measured and later transformed in the component of the force parallel to oscillations, $F_z(z)$, and interaction energy, $E(z)$, between tip and graphene [36]. Such measurements can be performed on the xy grid on the sample surface producing the 3D data sets, $\Delta f(x,y,z)$, which allows for a careful analysis of the data (see Fig. S4 and Movie S2 of the Supplemental Material [28]). Figure 3(a) (top panel) shows representative $\Delta f(z)$ curves extracted from such datasets for the middle positions of the respective high-symmetry places. The corresponding forces acting on the tip and the respective

tip-graphene interaction energy curves at different positions of the moiré structure are presented in the middle and the bottom panels, respectively. All sets show a clear depression on the attractive part of the curves for the ATOP positions. We can indicate the extremely good agreement between experimental and theoretical curves for $F_z(z)$ and $E(z)$. Simultaneously with the $\Delta f(z)$ signal, we also perform measurements of the so-called dissipation signal, $\Delta U(z) = \pi k A^2/Q(V/V_0 - 1)$ [37], which indicates the energy need in order to keep the oscillation amplitude constant [Fig. 3(b); see also Fig. S4 and Movie S3 of the Supplemental Material [28]]. Here k is the spring constant of the AFM sensor, A is the oscillation amplitude, V_0 driving voltage on the large z distance, and V actual driving voltage for the sensor. Several dissipative mechanisms might be responsible for this effect. In the present case, the most relevant one is the excitation of the movement of the graphene sheet due to the attractive interaction between graphene and the oscillating tip. One can clearly recognize two bumps on the curve for the dissipative channel for the ATOP positions. Each of these bumps is connected to the respective minima in the curve for the interaction force. The difference in the value for the dissipation energy between the ATOP and HCP/FCC positions is due to the weaker interaction between graphene and Ru for the ATOP position compared to HCP/FCC, which causes the smaller energy loss in keeping the oscillation amplitude constant.

Comparison of the obtained experimental results with the previously discussed DFT data shows very good agreement between theory and experiment (keeping in mind the complexity and size of the studied system consisting of 1140 atoms in the DFT simulations). Analyzing the $\Delta f(z)$ signal, we can take the difference between the positions of the first minima in the curve for the ATOP position and of the minima for the HCP position as a corrugation of the graphene on Ru(0001) that yields a value of 130 pm, which coincides with 127 pm obtained in DFT calculations.

Analysis of the force curves shows that subtraction of the long-range tail (originating from the macrotip) from the curve for the ATOP position gives for the first minima (in the first approximation) the reaction of the graphene nanobubble on the pressure from the tip side. The linear fit of the initial retraction part of this curve gives a stiffness of the graphene layer of 6.88 N/m, Young's modulus of 10.9 GPa, and finally a resonant frequency of approximately 0.74 THz (for details, see the Supplemental Material [28]). This value can be compared with the similar values of 10.6 N/m, 16.8 GPa, and 0.92 THz for graphene stiffness, Young's modulus, and the resonance frequency of graphene bubbles, respectively, obtained from the theoretical data [28]. Of course, the validity of the elastic theory for the continuous media might be questionable on the nanoscale, and further theoretical analysis is necessary. However, even this simplified approach gives very good agreement between experimental and theoretical data. The much smaller values for Young's modulus obtained in our study as compared to that measured for large graphene flakes of the μm size ($\approx$1 TPa) [38] can be explained by the presence of the Ru(0001) support in our experiments. In the former experiments, the graphene membrane was a freelike membrane [38]. In our case of the graphene nanodoms on Ru(0001), graphene cannot be considered as support-free, since even for the ATOP positions the distance between the graphene layer and the top Ru(S) layer is 3.415 Å. The closest value to the presently observed value of Young's modulus was obtained for SiO_2-supported graphene, 37 GPa [39]. Taking into account the calculated distance between graphene and SiO_2 of 2.8–3.5 Å [40,41], the obtained value in our experiment of Young's modulus for graphene on Ru(0001) at the ATOP positions correlates very well with the observed trend: Young's modulus is decreased due to the underlying substrate.

The reproducibility of the observed effect is demonstrated in Fig. 3(c) (see also Figs. S4 and S5, Movie S2, and Movie S3 of the Supplemental Material [28]), where several maps for the $\Delta f(z)$ and $\Delta U(z)$ channels measured in the constant height AFM mode for the graphene moiré lattice on Ru(0001) are shown, i.e., for the array of graphene nanoresonators. The cuts presented in Fig. S4 were extracted from the 3D sets of data, which were collected on the xy grid as discussed earlier. One can clearly see that all graphene nanobubbles in ATOP positions show the same nanodrum behavior with the same elastic properties. A similar effect was also observed in the pure constant height data for the $\Delta f(z)$ and $\Delta U(z)$ channels, as shown in Fig. 3(c) and Fig. S5 of the Supplemental Material [28]. As was demonstrated [42], such an assembly of graphene nanoresonators can be fabricated on the mm-size substrates, where all these nm-sized nanoresonators have the same characteristics and performance, which opens the high perspectives for application of such nanoresonator arrays in THz communication and biosensing [43].

IV. CONCLUSIONS

We performed an analysis of the crystallographic structure of the strongly corrugated graphene/Ru(0001) system employing a combination of state-of-the-art density-functional theory and scanning probe microscopy and spectroscopy (STM/AFM). Our force spectroscopy data demonstrate the unexpected two-minima behavior for the $\Delta f(z)$ and $F_z(z)$ channels for the ATOP places of the graphene/Ru(0001) structure that was successfully reproduced in the DFT calculations. We found that graphene at the ATOP places behaves like identical nanodrums (or nanoresonators) having a resonance frequency of about 1 THz and Young's modulus, which is much smaller compared to the one for the free-standing-like graphene membranes. Our analysis also allows us to directly extract the value of the graphene corrugation from the direct comparison of the $\Delta f(z)$ curves for different places of the graphene structure, which can be used in further applications of SPM for graphene-based systems.

ACKNOWLEDGMENTS

The High Performance Computing Network of Northern Germany (HLRN-III) is acknowledged for computer time. Financial support from the German Research Foundation (DFG) through Grant No. VO1711/3-1 within the Priority Programme 1459 "Graphene" is appreciated.

[1] L. A. Ponomarenko, R. V. Gorbachev, G. L. Yu, D. C. Elias, R. Jalil, A. A. Patel, A. Mishchenko, A. S. Mayorov, C. R. Woods, J. R. Wallbank, M. Mucha-Kruczynski, B. A. Piot, M. Potemski, I. V. Grigorieva, K. S. Novoselov, F. Guinea, V. I. Fal'ko, and A. K. Geim, Nature (London) **497**, 594 (2013).

[2] B. Hunt, J. D. Sanchez-Yamagishi, A. F. Young, M. Yankowitz, B. J. LeRoy, K. Watanabe, T. Taniguchi, P. Moon, M. Koshino, P. Jarillo-Herrero, and R. C. Ashoori, Science **340**, 1427 (2013).

[3] M. Yankowitz, J. Xue, D. Cormode, J. D. Sanchez-Yamagishi, K. Watanabe, T. Taniguchi, P. Jarillo-Herrero, P. Jacquod, and B. J. LeRoy, Nat. Phys. **8**, 382 (2012).

[4] P. Sutter, Y. Huang, and E. Sutter, Nano Lett. **14**, 4846 (2014).

[5] I. Pletikosić, M. Kralj, P. Pervan, R. Brako, J. Coraux, A. N'Diaye, C. Busse, and T. Michely, Phys. Rev. Lett. **102**, 056808 (2009).

[6] S. Rusponi, M. Papagno, P. Moras, S. Vlaic, M. Etzkorn, P. M. Sheverdyaeva, D. Pacilé, H. Brune, and C. Carbone, Phys. Rev. Lett. **105**, 246803 (2010).

[7] J. Xhie, K. Sattler, M. Ge, and N. Venkateswaran, Phys. Rev. B **47**, 15835 (1993).

[8] Z. Y. Rong and P. Kuiper, Phys. Rev. B **48**, 17427 (1993).

[9] P. Lauffer, K. V. Emtsev, R. Graupner, T. Seyller, L. Ley, S. A. Reshanov, and H. B. Weber, Phys. Rev. B **77**, 155426 (2008).

[10] F. Hiebel, P. Mallet, L. Magaud, and J. Y. Veuillen, Phys. Rev. B **80**, 235429 (2009).

[11] Yu. Dedkov, E. Voloshina, and M. Fonin, Phys. Status Solidi B **252**, 451 (2015).

[12] Yu. Dedkov and E. Voloshina, J. Phys.: Condens. Matter **27**, 303002 (2015).

[13] C. Busse, P. Lazić, R. Djemour, J. Coraux, T. Gerber, N. Atodiresei, V. Caciuc, R. Brako, A. T. N'Diaye, S. Blügel, J. Zegenhagen, and T. Michely, Phys. Rev. Lett. **107**, 036101 (2011).

[14] D. Stradi, S. Barja, C. Díaz, M. Garnica, B. Borca, J. J. Hinarejos, D. Sánchez-Portal, M. Alcamí, A. Arnau, A. L. Vázquez de Parga, R. Miranda, and F. Martín, Phys. Rev. Lett. **106**, 186102 (2011).

[15] E. N. Voloshina, Y. S. Dedkov, S. Torbrügge, A. Thissen, and M. Fonin, Appl. Phys. Lett. **100**, 241606 (2012).

[16] W. Moritz, B. Wang, M. L. Bocquet, T. Brugger, T. Greber, J. Wintterlin, and S. Gunther, Phys. Rev. Lett. **104**, 136102 (2010).

[17] E. N. Voloshina, E. Fertitta, A. Garhofer, F. Mittendorfer, M. Fonin, A. Thissen, and Y. S. Dedkov, Sci. Rep. **3**, 1072 (2013).

[18] S. K. Hämäläinen, M. P. Boneschanscher, P. H. Jacobse, I. Swart, K. Pussi, W. Moritz, J. Lahtinen, P. Liljeroth, and J. Sainio, Phys. Rev. B **88**, 201406 (2013).

[19] D. Stradi, S. Barja, C. Díaz, M. Garnica, B. Borca, J. J. Hinarejos, D. Sánchez-Portal, M. Alcamí, A. Arnau, A. L. Vázquez de Parga, R. Miranda, and F. Martín, Phys. Rev. B **85**, 121404 (2012).

[20] S. Sadewasser and M. C. Lux-Steiner, Phys. Rev. Lett. **91**, 266101 (2003).

[21] M. P. Boneschanscher, S. K. Hämäläinen, P. Liljeroth, and I. Swart, ACS Nano **8**, 3006 (2014).

[22] S. Koch, D. Stradi, E. Gnecco, S. Barja, S. Kawai, C. Díaz, M. Alcamí, F. Martín, A. L. V. de Parga, R. Miranda, T. Glatzel, and E. Meyer, ACS Nano **7**, 2927 (2013).

[23] P. E. Blöchl, Phys. Rev. B **50**, 17953 (1994).

[24] J. P. Perdew, K. Burke, and M. Ernzerhof, Phys. Rev. Lett. **77**, 3865 (1996).

[25] G. Kresse and J. Hafner, J Phys.: Condens. Matter **6**, 8245 (1994).

[26] S. Grimme, J. Comput. Chem. **27**, 1787 (2006).

[27] J. Tersoff and D. R. Hamann, Phys. Rev. B **31**, 805 (1985).

[28] See Supplemental Material at http://link.aps.org/supplemental/10.1103/PhysRevB.93.235418 for data analysis details, sample characterization by STM and AFM, and extended theoretical and experimental data sets.

[29] S. Marchini, S. Günther, and J. Wintterlin, Phys. Rev. B **76**, 075429 (2007).

[30] P. W. Sutter, J.-I. Flege, and E. A. Sutter, Nat. Mater. **7**, 406 (2008).

[31] D. Martoccia, P. R. Willmott, T. Brugger, M. Bjorck, S. Gunther, C. M. Schleputz, A. Cervellino, S. A. Pauli, B. D. Patterson, S. Marchini, J. Wintterlin, W. Moritz, and T. Greber, Phys. Rev. Lett. **101**, 126102 (2008).

[32] T. Brugger, S. Günther, B. Wang, H. Dil, M.-L. Bocquet, J. Osterwalder, J. Wintterlin, and T. Greber, Phys. Rev. B **79**, 045407 (2009).

[33] J. Lu, A. H. C. Neto, and K. P. Loh, Nat. Commun. **3**, 823 (2014).

[34] T. Mashoff, M. Pratzer, V. Geringer, T. J. Echtermeyer, M. C. Lemme, M. Liebmann, and M. Morgenstern, Nano Lett. **10**, 461 (2010).

[35] Z. Osváth, F. Lefloch, V. Bouchiat, and C. Chapelier, Nanoscale **5**, 10996 (2013).

[36] J. E. Sader and S. P. Jarvis, Appl. Phys. Lett. **84**, 1801 (2004).

[37] F. J. Giessibl, Rev. Mod. Phys. **75**, 949 (2003).

[38] C. Lee, X. Wei, J. W. Kysar, and J. Hone, Science **321**, 385 (2008).

[39] M. Poot and H. S. J. van der Zant, Appl. Phys. Lett. **92**, 063111 (2008).

[40] W. Gao, P. Xiao, G. Henkelman, K. M. Liechti, and R. Huang, J. Phys. D **47**, 255301 (2014).

[41] W. Wang, S. Li, J. Min, and C. Shen, J. Nanosci. Nanotechnol. **15**, 2970 (2015).

[42] Y. Pan, H. Zhang, D. Shi, J. Sun, S. Du, F. Liu, and H.-j. Gao, Adv. Mater. **21**, 2777 (2009).

[43] P. Tassin, T. Koschny, and C. M. Soukoulis, Science **341**, 620 (2013).